Journal of Cleaner Production 514 (2025) 145785

Contents lists available at ScienceDirect

Journal of Cleaner Production

journal homepage: www.elsevier.com/locate/jclepro

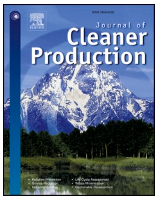

Juniperus pseudosabina extract-mediated green synthesis of zinc oxide artichoke-like structures for antibacterial applications

Zulfira Kurbanova [a], Sofia I.A. Pereira [b], Ana S.S. Sousa [b], Clara Piccirillo [c], Ulugbek Shaislamov [d], Kunio Yubuta [e], Katsuya Teshima [e], Thomas Eitinger [f], Mirabbos Hojamberdiev [a,g,*]

[a] *Institut für Chemie, Technische Universität Berlin, Straße des 17. Juni 135, 10623, Berlin, Germany*
[b] *Universidade Católica Portuguesa, CBQF - Centro de Biotecnologia e Química Fina – Laboratório Associado, Escola Superior de Biotecnologia, Rua Diogo Botelho 1327, 4169-005, Porto, Portugal*
[c] *Istituto di Nanotecnologia NANOTEC, Consiglio Nazionale delle Ricerche, Strada Provinciale Lecce-Monteroni, Campus Ecotekne, 73100, Lecce, Italy*
[d] *Center for Development of Nanotechnology at the National University of Uzbekistan, University Str. 4, 100174, Tashkent, Uzbekistan*
[e] *Institute for Aqua Regeneration, Shinshu University, 4-17-1 Wakasato, Nagano, 380-8553, Japan*
[f] *Institut für Biologie/Mikrobiologie, Humboldt-Universität zu Berlin, Unter den Linden 6, Berlin, 10099, Germany*
[g] *Mads Clausen Institute, University of Southern Denmark, Alsion 2, 6400, Sønderborg, Denmark*

ARTICLE INFO

Keywords:
Zinc oxide
Green synthesis
Plant extract
Juniperus pseudosabina
Antibacterial activity

ABSTRACT

The green synthesis of zinc oxide (ZnO) using plant extracts provides an environmentally friendly alternative to conventional chemical and physical methods. This study investigates the green synthesis of ZnO using *Juniperus pseudosabina (J. plseudosabina)* extract, eliminating the need for thermal treatment and pH adjustment with alkali metal hydroxides. ZnO nanoparticles are synthesized by varying the plant extract volume (0–20 mL) in a 95 mL aqueous solution of $Zn(NO_3)_2{\cdot}6H_2O$. The optimal ratio (5 mL extract) yields phase-pure ZnO with an artichoke-like morphology. The possible formation mechanism of these structures is discussed. Additionally, ZnO is modified with silver (Ag) at concentrations of 0–3 at% to improve antibacterial properties. Structural and morphological characterizations confirm the formation of phase-pure ZnO with high crystallinity. Viable plate count assays demonstrate that both non-modified and Ag-modified ZnO exhibited strong antibacterial activity against *Staphylococcus aureus* and *Escherichia coli*, achieving 99.999 % bacterial inactivation. These findings suggest that ZnO and Ag-modified ZnO synthesized using *J. pseudosabina* extract can be a sustainable antibacterial agent, supporting its application in biomedical and environmental fields.

1. Introduction

The widespread overuse of antibiotics has accelerated the evolution and proliferation of antibiotic-resistant strains. This escalating resistance poses a substantial threat to ecosystems and public health, necessitating alternative antimicrobial strategies (Serwecińska, 2020). A promising approach to addressing microbial resistance to antibiotics involves the application of metal and metal oxide nanoparticles, which reveal intrinsic antimicrobial properties. ZnO has been widely studied as a promising antibacterial agent due to its excellent antimicrobial activity, stability, availability, and biocompatibility, effectively targeting essential bacterial cellular components (Sirelkhatim et al., 2015). The antibacterial activity of ZnO is strongly influenced by its particle morphology, size, and dimensions (Babayevska et al., 2022), which are dependent on the synthesis method. These methods can be either physical (e.g., laser ablation (Gavrilenko et al., 2019)) or chemical (e.g., sol-gel (Aga et al., 2022)). For instance, Gavrilenko et al. (2019) synthesized ZnO nanoparticles by nanosecond pulsed laser ablation of a Zn target in water and air for biomedical applications. The resulting nanoparticles had a size of 18–26 nm formed in air and 12–21 nm in water, respectively. ZnO produced in air exhibited higher antibacterial activity due to its uniform distribution and larger surface area. Aga et al. (2022) synthesized ZnO nanoparticles at varying temperatures via a sol-gel method, observing a decrease in bandgap energy (from 3.34 eV to 3.27 eV) and an increase in crystal size (from 1.63 nm to 2.67 nm) with elevated temperatures. Moreover, their antibacterial activity under

---

* Corresponding author. Mads Clausen Institute, University of Southern Denmark, Alsion 2, 6400, Sønderborg, Denmark.
E-mail address: mirabbos@mci.sdu.dk (M. Hojamberdiev).

https://doi.org/10.1016/j.jclepro.2025.145785
Received 5 January 2025; Received in revised form 19 May 2025; Accepted 22 May 2025

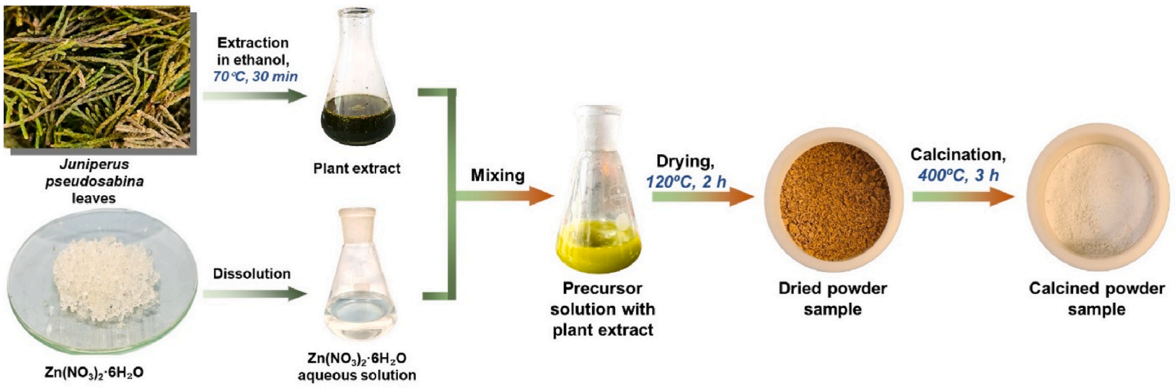

Fig. 1. Green synthesis process of ZnO powder using the plant extract of *J. pseudosabina*. (For interpretation of the references to color in this figure legend, the reader is referred to the Web version of this article.)

visible light against *Staphylococcus aureus* improved with increasing the synthesis temperature, supporting the hypothesis that ZnO nanoparticles with lower bandgap energy can exhibit enhanced antibacterial efficacy.

Additionally, the antibacterial activity of ZnO has been significantly enhanced through Ag modification (Rajendran and Mani, 2020). Ag-doped ZnO nanoparticles demonstrated superior antibacterial activity against *Escherichia coli* and *Enterococcus hirae* compared to pristine ZnO nanoparticles, surpassing even the standard antibiotic kanamycin in laboratory assays (Sampath et al., 2022). Furthermore, Ag/ZnO nanoparticles exhibited enhanced antimicrobial efficacy against the bacterial pathogens *Xanthomonas citri* and *Pseudomonas syringae*, as well as fungal species *Aspergillus niger* and *Aspergillus flavus*, outperforming the conventional antibacterial agent ampicillin and the antifungal drug amphotericin B (Jaffri and Ahmad, 2019).

The green synthesis of ZnO nanoparticles using plant extracts presents a sustainable alternative to conventional chemical and physical methods (Basnet et al., 2018; Al-darwesh et al., 2024). Specifically, functional groups in plant extracts, such as hydroxyl, carbonyl, and amine groups from flavonoids, alkaloids, terpenoids, and phenolics facilitate the uniform formation of ZnO particles through chelation and reduction processes, while also serving as capping and stabilizing agents (Greeshma and Thamizselvi, 2023; Tesfaye et al., 2023). The intrinsic variability in phytochemical composition across plant species critically determines the structural and morphological characteristics of the synthesized ZnO (Mardosaitė et al., 2021).

A comparative analysis of ZnO nanoparticles synthesized using various natural plant extracts is presented in Table S1. ZnO nanoparticles with well-defined spherical morphology and an average size of 14 nm synthesized via the coprecipitation method using garlic extract exhibited the largest inhibition zones against *S. aureus*, *E. coli*, and *Pseudomonas aeruginosa*, outperforming ZnO nanoparticles synthesized with basil and rosemary extracts (Stan et al., 2016). Similarly, hexagonal ZnO nanoparticles synthesized with *Lawsonia inermis* plant extract were more effective against *S. aureus* than rod-shaped ZnO nanoparticles likely attributed to their enhanced ability to penetrate bacterial membranes and induce cell leakage (Upadhyaya et al., 2018).

As a widely distributed evergreen conifer spanning regions from Central America to Tibet, *Juniperus* comprises 60–75 species with diverse phytochemical compositions (Fig. S1). (Hampe and Petit, 2010) A detailed analysis of the phytochemical profile of *Juniperus communis* (JcL) and *Juniperus oxycedrus* (JoxL) leaf extracts identified ellagic acid as a predominant compound with concentrations of 8133.83 ± 4.03 μg/g in JcL and 2890.05 ± 0.29 μg/g in JoxL. Additionally, (−)-epigallocatechin (1129.23 ± 3.66 μg/g) and kaempferol (179.87 ± 2.26 μg/g) were identified as major constituents (Mërtiri et al., 2024). Despite the extensive distribution of *Juniperus* species, only a limited number of studies have explored their application in the synthesis of metal and metal oxide nanoparticles (see Table S2). Notably, Ag nanoparticles synthesized with an average size of 25.50 nm using *J. communis* plant extract exhibited significant antibacterial activity against *P. aeruginosa, E. coli,* and *S. aureus* (Mahboub et al., 2020). However, the plant extract of *J. pseudosabina* has not been previously investigated for its potential in the green synthesis of metal or metal oxide nanoparticles.

Table 1
ZnO samples synthesized with different extract volumes and Ag content.

Sample name	Plant extract volume (mL)	Sample name	Ag content (%)
ZnO-PE0	0	ZnO-Ag0	0
ZnO-PE1	1	ZnO-Ag0.1	0.1
ZnO-PE5	5	ZnO-Ag0.25	0.25
ZnO-PE10	10	ZnO-Ag0.5	0.5
ZnO-PE15	15	ZnO-Ag1	1
ZnO-PE20	20	ZnO-Ag3	20

Therefore, this study focuses on the green synthesis of ZnO using the plant extract of *J. pseudosabina.* The influence of plant extract volume variation and Ag concentration on the formation, particle morphology and size, and antibacterial activity of ZnO are investigated. The potential formation mechanism of ZnO under green synthesis conditions using *J. pseudosabina* plant extract is also discussed.

2. Experimental

2.1. Materials

Zinc nitrate hexahydrate (Zn(NO$_3$)$_2$·6H$_2$O, 99 %, Fluka), silver nitrate (AgNO$_3$, 99 %, Ferak), sodium hydroxide (NaOH, 99 %, Merck), ethanol (99 %, Merck), deionized water, and fresh leaves of *J. pseudosabina* collected from Almaty region, Kazakhstan.

2.2. Plant extract preparation and green synthesis of non-modified and Ag-modified ZnO

To prepare the plant extract, fresh leaves (10 g) of *J. pseudosabina* were blended and boiled in 100 mL ethanol at 50 °C for 30 min. The mixture was filtered using a Whatman® Grade 1 qualitative filter paper to remove a solid residue, and the plant extract was obtained.

In the green synthesis of non-modified ZnO (Fig. 1), the plant extract of *J. pseudosabina* (20 mL) was mixed with deionized water (80 mL) containing 0.1 M Zn(NO$_3$)$_2$·6H$_2$O. The mixture was stirred at room temperature for 5 min, dried at 120 °C for 1 h, and calcined at 400 °C for 3 h. The plant extract volume was varied (1, 5, 10, 15, and 20 mL) to investigate its effect on the morphology and size of ZnO. The samples were denoted as ZnO-PE1, ZnO-PE5, ZnO-PE10, ZnO-PE15, and ZnO-PE20 according to the plant extract volume used in the green synthesis process (see Table 1). For the comparison, ZnO was also synthesized without using the plant extract but by adding 0.05 M NaOH to 0.1 M $Zn(NO_3)_2 \cdot 6H_2O$ in 100 mL deionized water, heating to 70 °C for 30 min under magnetic stirring, washing the precipitate three times with deionized water, drying at 120 °C for 1 h, and calcining at 400 °C for 3 h. The sample was labeled as ZnO-PE0.

To modify ZnO with Ag nanoparticles, the same synthesis process of non-modified ZnO was applied by fixing the plant extract volume to 5 mL and adding $AgNO_3$ with different concentrations (0 at%, 0.1 at%, 0.25 at%, 0.5 at%, 1 at%, and 3 at% Ag) into the $Zn(NO_3)_2 \cdot 6H_2O$ aqueous solution. The samples were denoted as ZnO-Ag0, ZnO-Ag0.1, ZnO-Ag0.25, ZnO-Ag0.5, ZnO-Ag1, and ZnO-Ag3 according to the Ag concentration (Table 1).

2.3. Materials characterization

The X-ray diffraction (XRD) patterns of the samples were acquired with a PANalytical X'Pert PRO diffractometer with Cu $K\alpha$ radiation. The average crystallite size (D) was estimated using the Scherrer equation (Scherrer, 1918), and microstrain and dislocation density were also calculated (Khorsand Zak et al., 2011; Devamani and Alagar, 2013). The morphology and size of the samples were analyzed using a Carl Zeiss LEO982 scanning electron microscope. The elemental composition of the samples was analyzed by energy-dispersive X-ray spectroscopy (EDS; DSM 982 GEMINI, Carl Zeiss, with a Bruker Quantax XFlash® 6|60). The bright-field (BF) TEM images and selected-area electron diffraction (SAED) patterns and lattice images were observed by a transmission electron microscope (TEM, JEM-2100F, JEOL) equipped with CETCOR (CEOS GmbH) operating at an acceleration voltage of 80 kV. The surface chemical composition and states of elements in the samples were analyzed by X-ray photoelectron spectroscopy (XPS; JPS-9010MX, JEOL) using non-monochromatic Mg-Kα radiation. The XPS spectra were fitted by Gaussian-Lorentzian functions and all XPS spectra were corrected for possible charging effects according to the C 1s peak. The ultraviolet–visible (UV–Vis) diffuse reflectance spectra of the samples were recorded with an Evolution 220 UV/Vis spectrometer (Thermo Fisher Scientific) in the wavelength range of 200–800 nm. The optical band gap energy was estimated using the Tauc method (Makuła et al., 2018). The surface charge of the powders was determined using a Dynamic Light Scattering instrument (NanoZS90), with a concentration of 1 mg/mL in distilled water.

2.4. Antibacterial activity tests

Agar-based disk-diffusion assay. Indicator strains *Bacillus subtilis* 168 and *E. coli* W3110 were cultured overnight in lysogeny broth (LB - 1 % tryptone, 0.5 % yeast extract, and 0.25 % NaCl). LB agar plates were overlaid with 5 mL molten LB soft agar (0.6 % agar) immediately after inoculation with 200 μL of the bacterial suspensions. Paper disks (6 mm) soaked with 20 μL of the suspension of non-modified or Ag-modified ZnO powder in dimethyl sulfoxide (DMSO) were placed on the plates, the plates were incubated at 30 °C for 2 days, and photographed to measure the diameter of the inhibition areas.

Bacterial viable plate count method. In this assay, the Gram-positive bacteria *Staphylococcus aureus* ATCC6538 and the Gram-negative bacteria *Escherichia coli* ATCC 25922 were used. Both *S. aureus* and *E. coli* were grown overnight in Mueller-Hinton agar media (Biokar) at 37°C. Liquid suspensions of each bacterial strain were prepared in sterile saline isotonic solution (NaCl 0.85 %), with an approximate concentration of 10^7-10^8 cfu/mL. A volume of 800 μL from each suspension was added to a sterile Petri dish, along with 7.2 mL of sterile saline solution. Selected amounts of sample powder (1 mg/mL and 0.5 mg/mL) were added to the Petri dish; to avoid contamination, the powders were sterilized by placing them at 100 °C overnight.

The petri dishes were gently shaken (80 rpm) for 5 h; after this time, aliquots were taken from the suspension and diluted using sterile saline solution; the diluted solution was plated into Plate Counting Agar (PCA; Merck) and incubated at 37 °C for 24–48 h. After this, the colonies forming units (CFU) were counted. Control experiments were performed considering only the bacterial suspension, with no powdery sample added. Each test was performed in triplicate; an average value for the cfu was considered, with the associated standard deviation.

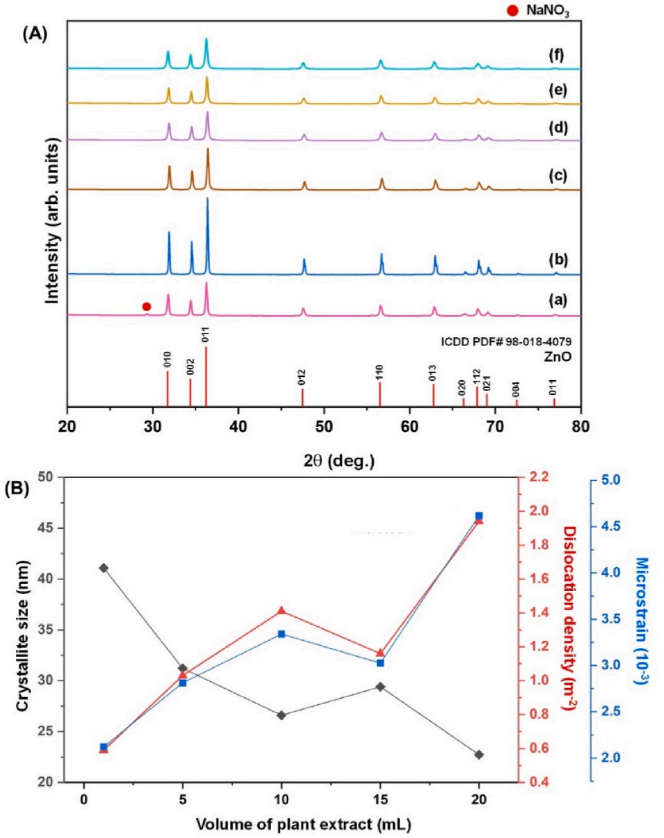

Fig. 2. (A) XRD patterns of ZnO powder synthesized using different volumes of *J. pseudosabina* plant extract in ethanol: (a) without extract, (b) 1 mL, (c) 5 mL, (d) 10 mL, (e) 15 mL, and (f) 20 mL. (B) Crystallite size (black circles, left axis), dislocation density (red triangles, right axis), and microstrain (blue square, right axis) of ZnO powder synthesized using different volumes of *J. pseudosabina* plant extract in ethanol. (For interpretation of the references to color in this figure legend, the reader is referred to the Web version of this article.)

To explain the antibacterial behavior of each sample, the release of Zn and Ag ions was measured at the end of the test, using an Inductively Coupled Plasma Optical Emission Spectrometer (ICP-OES) Avio™ 220 Max (PerkinElmer).

Estimation of minimum inhibitory concentration (MIC). To determine the MICs of ZnO-PE5 and ZnO-Ag.025 against Gram-positive *Bacillus subtilis* 168 and Gram-negative *Escherichia coli* W3110, the suspensions of ZnO-PE5 and ZnO-Ag.025 were added to non-turbid bacterial suspensions in LB medium, resulting in final inhibitor concentrations ranging from 25 to 800 μg/mL. The MICs were estimated as the lowest concentration that prevented an increase in turbidity upon overnight incubation at 30 °C under shaking. Survivors in non-turbid samples were quantified by spreading aliquots onto ZnO-free LB agar plates.

3. Results and discussion

3.1. Characterization of ZnO synthesized using different plant extract volumes and Ag concentrations

To assess the impact of plant extract volume on the formation, particle morphology, and size of ZnO, the volume of *J. pseudosabina* plant

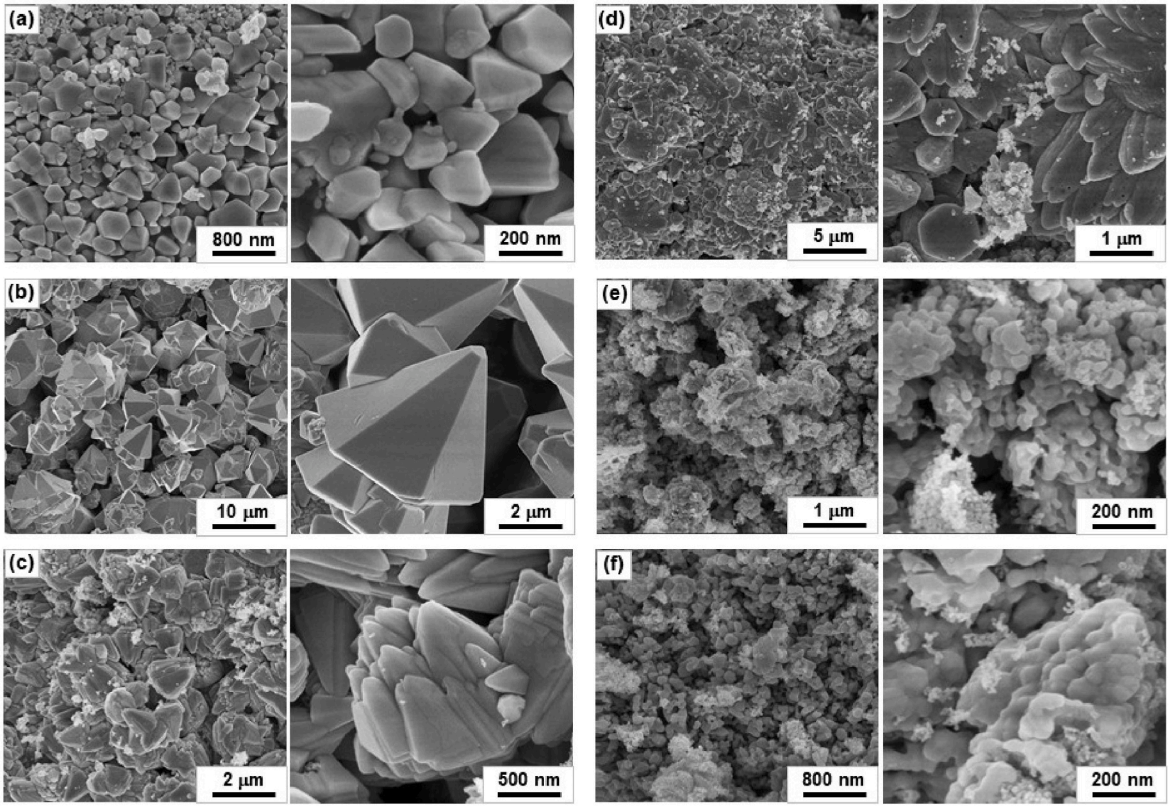

Fig. 3. SEM images of ZnO powder synthesized using different volumes of *J. pseudosabina* plant extract in ethanol: (a) without extract, (b) 1 mL, (c) 5 mL, (d) 10 mL, (e) 15 mL, and (f) 20 mL.

extract in ethanol solution was varied (1, 5, 10, 15, and 20 mL). The XRD patterns of ZnO samples synthesized without and with *J. pseudosabina* plant extract in varying volumes (1–20 mL) are shown in Fig. 2A. In the XRD patterns, the predominant reflections at $2\theta = 31.7^\circ$, 34.4°, 36.2°, 47.5°, 56.5°, 62.8°, 66.3°, 67.8°, 69.0°, 72.5°, 76.8°, 81.3°, and 89.5° correspond to the (010), (002), (011), (012), (110), (013), (020), (112), (021), (004), and (011) crystallographic planes of würtzite-type ZnO crystallizing in the hexagonal $P6_3mc$ space group (ICDD PDF card number: 98-018-4079). The high intensity of reflections and the absence of extra reflections in the XRD patterns of ZnO powder synthesized with *J. pseudosabina* plant extract indicate its high crystallinity and phase purity, respectively. In contrast, the XRD pattern of ZnO powder synthesized without plant extract, which required pH adjustment with NaOH and thermal treatment during solution processing, shows a small reflection assignable to $NaNO_3$ (ICDD PDF card number: 01-072-1213). This highlights the advantage of using *J. pseudosabina* plant extract for the green synthesis of ZnO without the addition of NaOH and thermal treatment during the solution processing.

The unit-cell parameters, average crystallite sizes, microstrain, and dislocation density of ZnO synthesized with different volumes of *J. pseudosabina* plant extract are shown in Table S3. The unit-cell parameters, including the c/a ratio and unit-cell volume, closely match the standard values for the würtzite-type ZnO structure (ICDD PDF card number: 98-018-4079). Overall, with increasing the volume of plant extract, the crystallite size tends to decrease, as they go from 41.08 nm (sample ZnO-PE1) to 22.73 nm (sample ZnO-PE20). The only exception to this trend is observed for sample ZnO-PE15, whose average crystallite size is 29.41 nm (i.e. larger than ZnO-PE10, see Fig. 2B and Table S3). These data indicate that increasing the volume of plant extract promotes the formation of smaller crystals due to controlled nucleation and crystal growth facilitated by phytochemicals acting as capping agents. As expected, the microstrain increases from 1.45 to 1.51 as the crystallite size of ZnO decreases owing to the higher surface-to-volume ratio, causing a lattice distortion and internal strain. Similarly, the dislocation density increases from 0.59 to 1.94 ($\times 10^{-3}$ m^{-2}) with a decrease in the crystallite size, driven by increased defect density and surface energy. These results are consistent with the findings of a previous study (Khorsand Zak et al., 2011), where the increase in microstrain was observed with smaller sizes of ZnO particles by applying the Williamson-Hall (W-H) and size-strain plot methods.

The scanning electron microscopy (SEM) images of ZnO synthesized without plant extract (Fig. 3a) reveal a mixed morphology, including spherical, hexagonal, and pyramidal crystals, with an average size of about 200 nm. When the extract volume was set to 1 mL, uniform hexagonal pyramid-like structures with smooth and triangular faces were formed, averaging 2.22 μm in diameter and 5.3 μm in length (Fig. 3b). Increasing the extract volume to 5 mL (Fig. 3c) resulted in the formation of artichoke-like structures, which are characterized by petal-shaped growth along the c-axis, with an average size of 1.14 μm. With a 10-mL extract volume (Fig. 3d), the morphology changed to predominantly dense flower-like and hexagonal structures with an average size of 1.33 μm. When the extract volume was further adjusted to 15 mL (Fig. 3e), the ZnO with aggregated, elongated, and semi-spherical shapes with an average size of 195 nm was formed. Finally, at a 20-mL extract volume (Fig. 3f), dense clusters and intertwined structures with an average size of 135 nm were observed, suggesting that lower and higher extract volumes could promote the growth of large and idiomorphic crystals and the reduction in the crystallite size and aggregation, respectively.

Li et al. (1999) suggested that the variation in crystal growth behavior across different morphologies is linked to the growth rate of crystal faces, which depends on the orientation of the coordination polyhedron at the interface. For the würtzite-structured ZnO crystals, which consist of alternating planes of tetrahedrally-coordinated Zn^{2+} and O^{2-} ions, the growth rate is fastest for crystal faces with a polyhedral corner at the interface, followed by those with an edge. Crystals

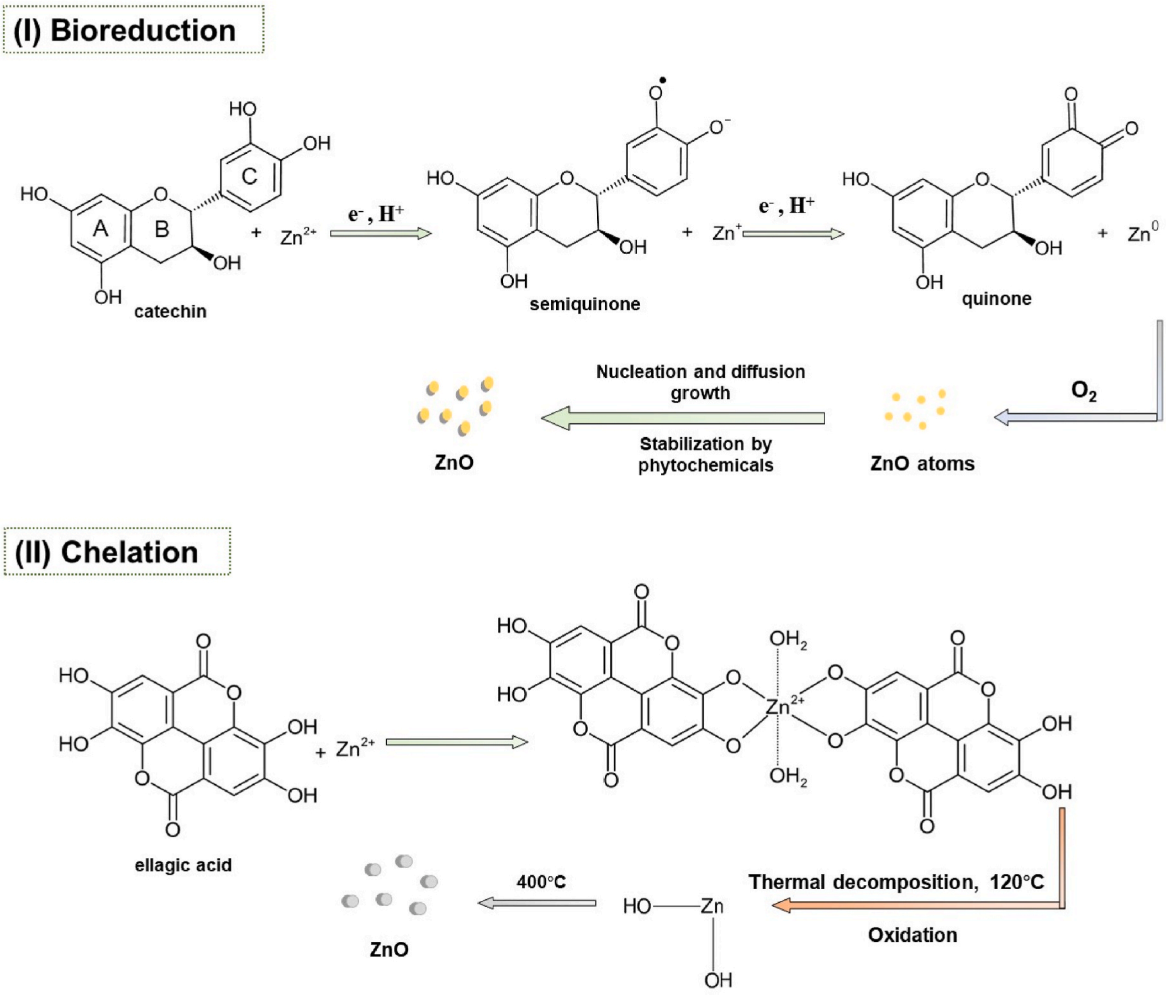

Fig. 4. Possible mechanisms of the formation of ZnO under green synthesis conditions using *J. pseudosabina* plant extract. (For interpretation of the references to color in this figure legend, the reader is referred to the Web version of this article.)

with polyhedral faces at the interface grow the slowest. Thus, the growth rate of ZnO crystals in different directions follows the order: $V_{[0001]} > V_{[01\bar{1}\bar{1}]} > V_{[01\bar{1}0]} > V_{[000\bar{1}]}$, which indicates that the fastest growth rate is in the [0001] direction (*c*-axis) (Li et al., 1999). Crystal faces with slower growth rates tend to remain, while those with faster growth rates are more likely to disappear. The disappearance of the (0001) crystal face can result in elongated petal structures, leading to an artichoke-like morphology (Fig. 3c and d).

It is known that the orientation of surface planes and the exposure of specific crystal faces in materials play a crucial role in determining their functional properties. These variations can greatly impact a material's surface energy, availability of active sites, and efficiency of charge separation, thus influencing its overall characteristics, including photocatalytic and antibacterial activities. Therefore, understanding the contributions of distinct exposed facets is essential for the rational design of advanced photocatalysts and antibacterial agents. In anatase TiO_2, the low-index facets, such as {001}, {010}, and {101}, exhibited distinct properties, and the {001} facet was identified as the most photocatalytically active one due to its higher surface energy, higher density of under-coordinated Ti and O atoms that serve as catalytic sites, strong adsorption affinity for reactant molecules, and its efficient charge carrier separation that enhances the photocatalytic activity (Ong et al., 2014). Wang et al. (2011) successfully synthesized decahedral $BiVO_4$ crystals with dominant (040) facets by hydrothermal methods, and the photocatalytic activity for water oxidation was proportionally correlated well with the extent of the (040) facet growth. By controlling the kinetics of crystal growth, Zhao et al. (2017) achieved efficient photocatalytic water oxidation for decahedral $BiVO_4$ crystals with specific configurations of the {010} and {011} exposed facets. Talebian et al. (2013) synthesized ZnO structures with diverse morphologies and found that flower-like ZnO structures can exhibit significantly higher photocatalytic inactivation than rod- and sphere-like ZnO structures against *E. coli* in comparison to *S. aureus* due to the dominance of (002) facet with a higher surface energy and a greater number of oxygen vacancies. Yubuta et al. (2007) examined the morphology of ZnO fibers by means of scanning and transmission electron microscopy and found that the ZnO fibers consist of ZnO micro-rods constructed from nano-crystals with high crystallinity, which are connected without definite orientation relations.

The plant extract of *J. pseudosabina* contains various active compounds, notably polyphenols like ellagic acid, catechin, kaempferol, and quercetin, which are known for their antioxidant and antibacterial properties (Mërtiri et al., 2024). Polyphenols and flavonoids exhibit these properties through aromatic hydroxyl groups that act as radical scavengers. The complex composition of these compounds makes it difficult to quantify the specific molecules and to understand the formation pathways of ZnO using such extracts. Despite this, two main possible mechanisms for the formation of ZnO under green synthesis conditions using the plant extract of *J. pseudosabina* are proposed:

(i) Bioreduction: The extracted plant phytochemicals with phenolic compounds reduce Zn^{2+} to Zn^0 through electron transfer (Fig. 4).

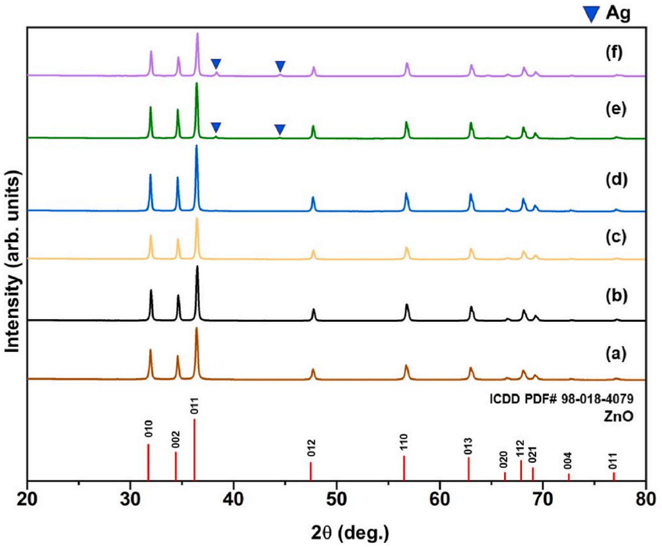

Fig. 5. XRD patterns of ZnO powder synthesized using a 5-mL plant extract of *J. pseudosabina* and different concentrations of Ag: (a) 0 at%, (b) 0.1 at%, (c) 0.25 at%, (d) 0.5 at%, (e) 1 at%, and (f) 3 at%.

Phenols donate electrons to metal ions, forming phenoxyl radicals. Janeiro et al. (Janeiro and Brett, 2004) found that (+)-catechin, with catechol (ring C), resorcinol groups (ring A), and hydroxyl group (ring B), transfers electrons primarily from the catechol ring due to its lower redox potential. This process involves electron and proton release, enhancing the antioxidant activity. Zn^{2+} is reduced to Zn^0 by accepting electrons from catechin, forming an intermediate (Zn^+). Finally, the ZnO nucleates and grows in the presence of dissolved oxygen during drying and calcination, respectively, with phytochemicals acting as capping agents to stabilize the ZnO crystals.

(ii) Chelation: the Zn^{2+} ions, with a closed shell d^{10} electron configuration, form tetrahedral, octahedral, and other complex structures. Their high positive charge density promotes a binding to phenolic acids. The chelation ability of polyphenols is influenced by catechol moieties and the arrangement of hydroxyl and carbonyl groups (Zhi Zing et al., 2022). Fig. 4 shows the formation of a Zn complex with ellagic acid. The Zn^{2+} ions bind to polyphenols through the oxophilic attraction with deprotonated oxygen atoms, forming stable rings. During the solution process and drying at 120 °C, an OH–Zn–OH intermediate is formed, which is converted to ZnO during calcination at 400 °C.

Based on the discussion above, it can be proposed that with a 1-mL plant extract, the limited availability of -OH groups from polyphenols leads to the bioreduction and the rapid formation of ZnO nuclei but a slower crystal growth (Fig. 3b). At higher extract volumes (5 and 10 mL), more OH groups increase the supersaturation and the formation of the zinc complex, resulting in the growth of more complex, branched structures, including artichoke-like morphologies (Fig. 3c and d). At the highest extract volumes (15 and 20 mL), the availability of Zn^{2+} ions decreases, dominating the intermediate complexes that are converted into ZnO with aggregated, elongated, and semi-spherical shapes (Fig. 3e and f).

The FTIR analysis was conducted to identify phytochemicals and their functional groups in the plant extract of *J. pseudosabina*, which are actively involved in the green synthesis of ZnO. The FTIR spectra of the sample, synthesized using a 5-mL plant extract, before and after calcination are shown in Fig. S2. Before calcination, a broad band at 3300–3500 cm^{-1} indicates the presence of –OH groups, confirming the possible presence of phytochemicals, such as alkaloids, flavonoids, and polyphenols. The band at 1640–1720 cm^{-1} corresponds to the –C=O

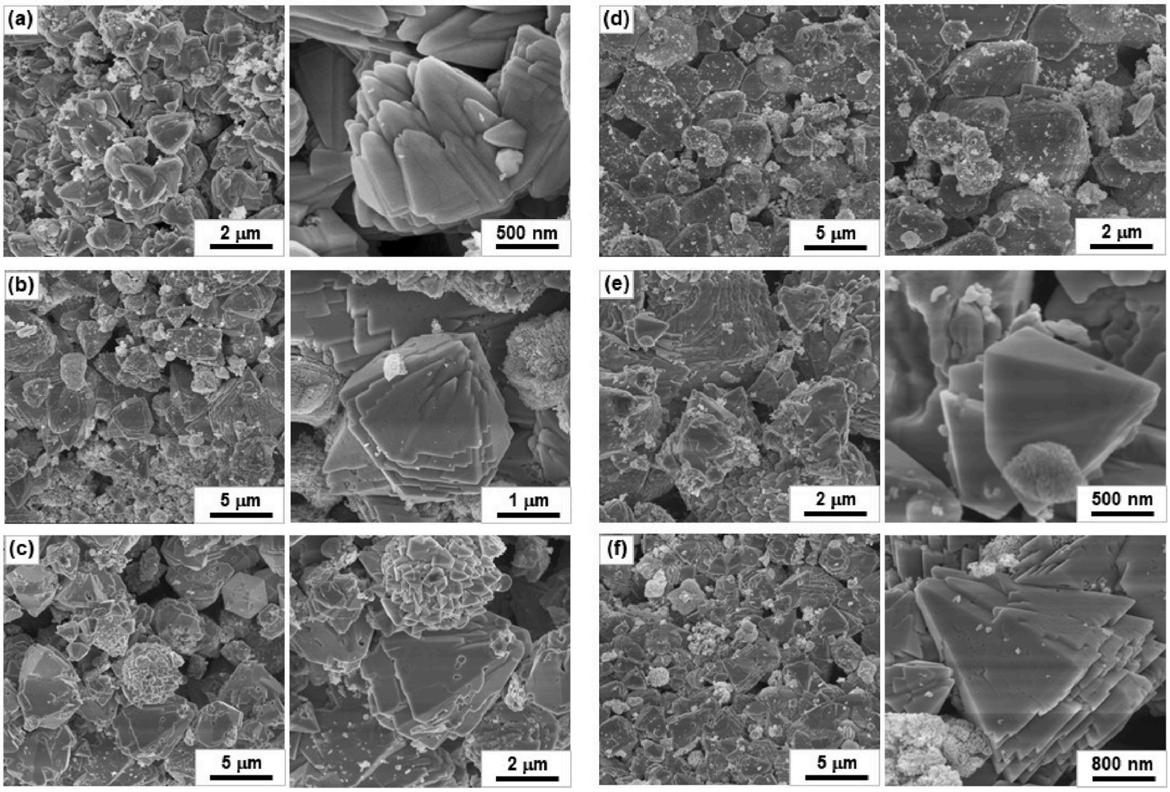

Fig. 6. SEM images of ZnO powder synthesized using a 5-mL plant extract of *J. pseudosabina* and different concentrations of Ag: (a) 0 at%, (b) 0.1 at%, (c) 0.25 at%, (d) 0.5 at%, (e) 1 at%, and (f) 3 at%.

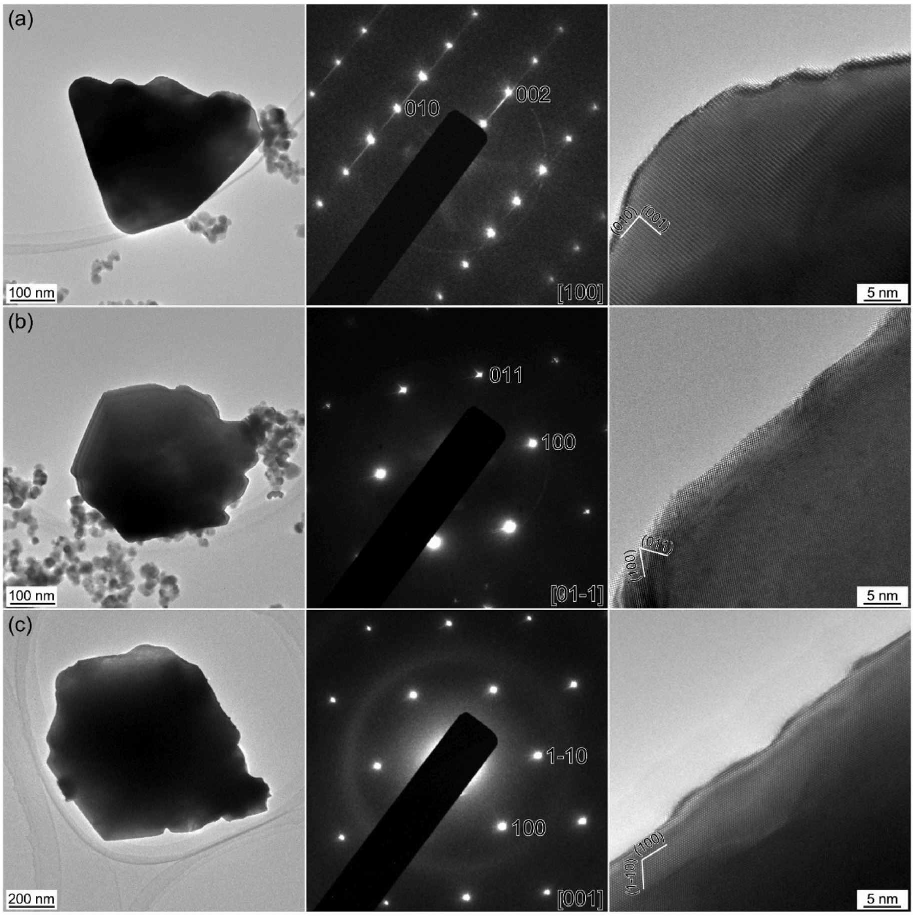

Fig. 7. Bright-field TEM images (*left*) and SAED patterns (*middle*) and HRTEM images (*right*) of ZnO powder synthesized using a 5-mL plant extract of *J. pseudosabina* and different concentrations of Ag: (a) 0 at%, (b) 0.25 at%, and (c) 3 at%.

stretching, aligning with the proposed bioreduction mechanism. The bands at 1490–1500 cm^{-1} are assigned to the C=C stretching in aromatic rings, while the bands at 1400–1420 cm^{-1}, 1300 cm^{-1}, and 1050 cm^{-1} are associated with the C–H bending, C–O stretching in alcohols or carboxylic acids, and C–O stretching in ethers, respectively. The Zn–O stretching is observed at the band at 750 cm^{-1}. After calcination, most phytochemical-related bands disappear, highlighting their essential roles in the formation of ZnO during the solution process and drying. Only the bands assignable to OH, C–O, and Zn–O remain due to atmospheric moisture, residual carbon, and the formed ZnO, respectively.

Next, ZnO was modified with Ag at different concentrations (0-3 at %) under green synthesis conditions using a 5-mL plant extract of *J. pseudosabina.* Due to the artichoke-like structures the modifications are expected to be beneficial for antibacterial activity. As shown in the XRD patterns in Fig. 5, the predominant reflections can be readily assigned to the hexagonal crystal structure of würtzite-type ZnO with space group *P*63*mc* (ICDD PDF card number 98-018-4079). The XRD patterns show intense and narrow reflections, suggesting the high crystallinity of Ag-modified ZnO. At higher concentrations of Ag (1 at% and 3 at%), the additional reflections appear at $2\theta = 38.20^\circ$ and 44.40°, which correspond to the (111) and (002) crystallographic planes of metallic Ag (ICDD PDF card number 98-006-4997). The appearance of additional reflections belonging to metallic Ag confirms the segregation of a secondary phase (metallic Ag), of which the intensity is further increased upon increasing the concentration of Ag.

The unit-cell parameters, average crystallite sizes, microstrain, and dislocation density of ZnO synthesized using a 5-mL plant extract of *J. pseudosabina* and different concentrations of Ag are shown in Table S4. The unit-cell parameters of ZnO show a non-monotonic trend with increasing the concentration of Ag. These parameters are consistent with the standard values of würtzite-type ZnO ($a = 0.3249$ nm, $c = 0.5207$ nm, $c/a = 1.63$, $V = 47.40$ Å^3). The unit-cell volume expands as the Ag concentration increases from 0.1 at% to 0.5 at% (ZnO-Ag0.1 to ZnO-Ag0.5) but decreases at 1 at% Ag and 3 at% Ag (ZnO-Ag1 to ZnO-Ag3). This may be due to the incorporation of Ag$^+$ at lower concentrations and the segregation of Ag^0 at higher concentrations, respectively. The Zn^{2+} ions have a four-fold coordination with an ionic radius of 0.6 Å, while Ag$^+$ has a radius of 1.26 Å. Having a larger ionic radius, Ag$^+$ substituted for Zn^{2+} in the ZnO lattice is expected to cause a lattice distortion. Volnianska et al. (2009) pointed out that the Ag$^+$ substitution for Zn^{2+} is favored in oxygen-rich conditions, while the Ag$^+$ substitution for O^{2-} is likely under oxygen-deficient conditions. A non-significant increase in the unit-cell parameters upon Ag$^+$ substitution at lower concentrations suggests that the Ag concentration was too low to cause noticeable changes. A decrease in microstrain with increasing the concentration of Ag presumably resulted from larger crystallite sizes and the formation of a secondary phase (metallic Ag). The XRD data show that the incorporation of Ag$^+$ into the ZnO lattice occurs at lower concentrations of Ag, while the segregation of the secondary phase (metallic Ag) takes place at higher concentrations of Ag.

The morphology, particle size, and growth mechanisms of ZnO modified with different concentrations of Ag were examined by SEM (Fig. 6). Non-modified ZnO (ZnO-PE5, renamed as ZnO-Ag0 hereafter) has artichoke-like structures with an average size of 1.14 μm (Fig. 6a). The ZnO-Ag0.1 sample, modified with 0.1 at% Ag, shows denser and more compact layered structures with an average diameter of 2.89 μm, and the petals have tightly connected tips (Fig. 6b). Increasing the concentration of Ag to 0.25 at% (ZnO-Ag0.25) promotes secondary

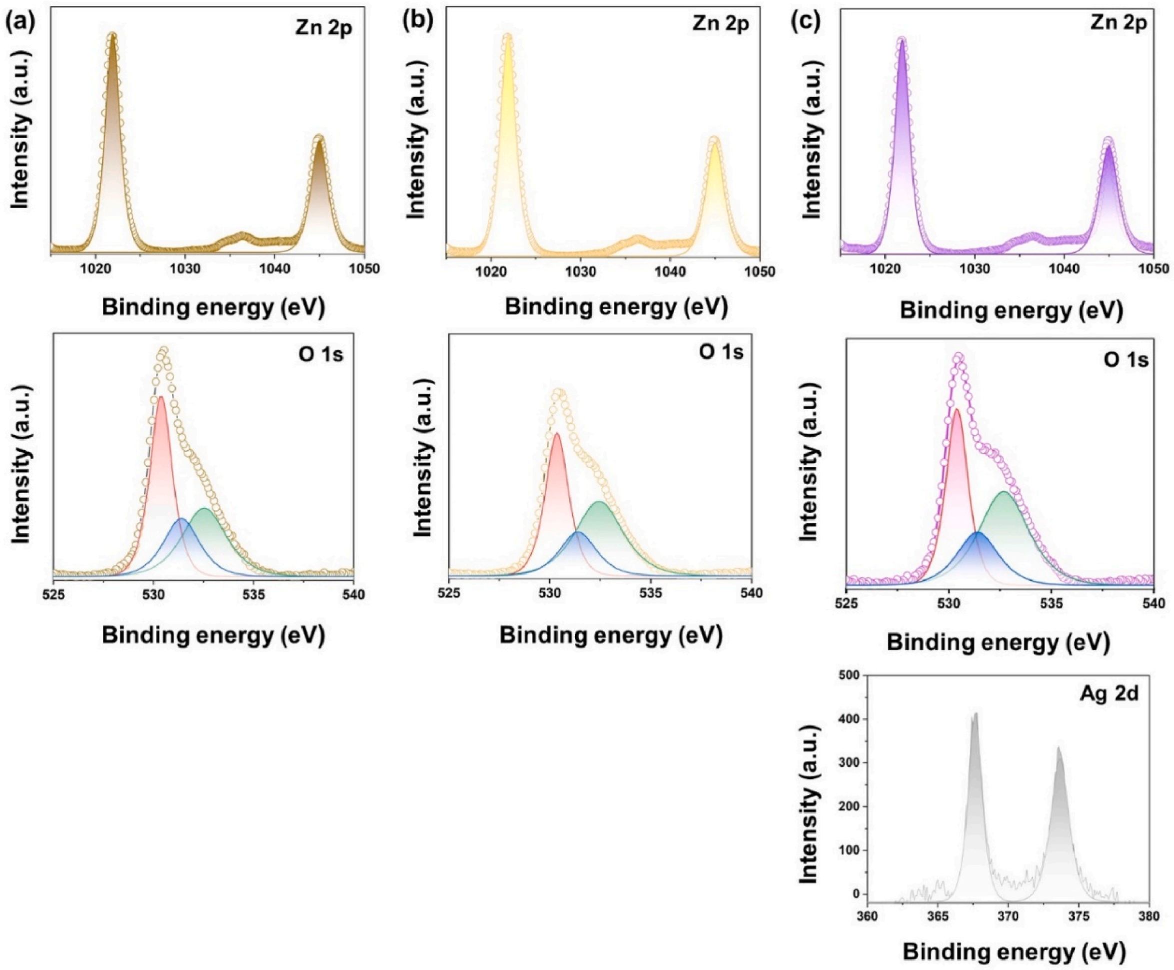

Fig. 8. Zn 2p (*top*), O 1s (*middle*), and Ag 2d (*bottom*) XPS spectra of ZnO powder synthesized using a 5-mL plant extract of *J. pseudosabina* and different concentrations of Ag: (a) 0 at%, (b) 0.25 at%, and (c) 3 at%.

nucleation on existing crystals, with an average size of 2.96 μm (Fig. 6c). This secondary nucleation is influenced by changes in thermodynamics and surface free energy, disrupting typical Ostwald ripening. The ZnO samples with 0.5 at% Ag (ZnO-Ag0.5) and 1 at% Ag (ZnO-Ag1) have hexagonal nanodisks and pyramidal particles with average sizes of 3.8 μm and 2.62 μm, respectively, indicating the layered patterns of crystal growth (Fig. 6d and e). At 3 at% Ag concentration, the ZnO-Ag3 sample has a layered morphology with some perturbations and an average size of 2.56 μm (Fig. 6f).

Energy-dispersive X-ray spectroscopy (EDS) was used to analyze the elemental composition and distribution in ZnO. The EDS spectra are shown in Fig. S3. For ZnO-Ag0 (Fig. S3a), the peaks of Zn and O confirm the presence of pure ZnO. In ZnO-Ag0.1 (Fig. S3b), the peak assignable to metallic Ag is absent because of its low concentration. Nevertheless, the peaks of Ag appear in the EDS spectra for ZnO samples with higher concentrations of Ag (0.25 at%, 0.5 at%, and 1 at%), confirming the successful modification of ZnO with Ag (Fig. S3c–e). For ZnO-Ag3, an intense peak of Ag suggests the formation of a secondary phase – metallic Ag (Fig. S3f). The EDS element mapping images of ZnO-Ag3 in Fig. S4 confirm the formation of Ag clusters on the surface of ZnO at 3 at% Ag concentration.

Fig. 7 shows the bright-field TEM images, SAED patterns, and HRTEM images of ZnO powder synthesized using a 5-mL plant extract of *J. pseudosabina* and different concentrations of Ag: (a) 0 at%, (b) 0.25 at%, and (c) 3 at%. The sharp diffraction spots in SAED patterns (center panels of Fig. 7) and the sharp crystal planes (left panels of Fig. 7), i.e., facets, appear on the edges of the samples, indicating their high crystallinity. In the HRTEM images on the right panels of Fig. 7, no structural defects, such as point defects, and dislocations, can be observed. The interplanar spacings of (001), (100), and (011) planes in the HRTEM images are estimated to be 0.521 nm, 0.282 nm, and 0.246 nm, respectively. These values are very close to those of 0.521 nm, 0.281 nm, and 0.245 nm, respectively, based on the lattice constants.

The surface chemical composition and oxidation states of elements of non-modified ZnO (ZnO-Ag0) and Ag-modified ZnO with Ag concentrations of 0.25 at% and 3 at% (ZnO-Ag0.25 and ZnO-Ag3) were analyzed by XPS. Fig. S5 shows the XPS survey spectra for these three samples, indicating the characteristic peaks of Zn, O, and Ag. The Ag peak is notable only in the ZnO-Ag3 sample, and the C 1s peak confirms the presence of adventitious carbon. Fig. 8 shows the Zn 2p and O 1s XPS spectra of ZnO-Ag0, ZnO-Ag0.25, and ZnO-Ag3. In the Zn 2p XPS spectra, the peaks at 1045.4 eV, 1021.5 eV, 141.0 eV, and 89.8 eV are attributed to the electronic transitions of Zn $2p_{1/2}$, Zn $2p_{3/2}$, Zn $3s_{1/2}$, and Zn $3p_{3/2}$, respectively (Al-Gaashani et al., 2013). For the ZnO-Ag0 (Fig. 8a), the binding energies of Zn $2p_{3/2}$ and Zn $2p_{1/2}$ are found to be 1021.93 eV and 1045.03 eV, respectively. For the ZnO-Ag0.25 and ZnO-Ag3 (Fig. 8b and c), these binding energies are located at 1021.87 eV and 1044.97 eV, 1021.87 eV and 1044.98 eV, respectively. The core-level binding energy difference for Zn 2p is approximately 23.1 eV for all samples, indicating the oxidation state of +2 for Zn. The deconvolution of the O 1s peak reveals three components: lattice oxygen (O_L) at 530.42 eV, oxygen vacancies (O_V) at 531.43 eV, and surface-adsorbed oxygen (O_A) at 532.52 eV (Mintcheva et al., 2018). No Ag 3d peak is observed for ZnO-Ag0.25 due to its low concentration. In contrast, the

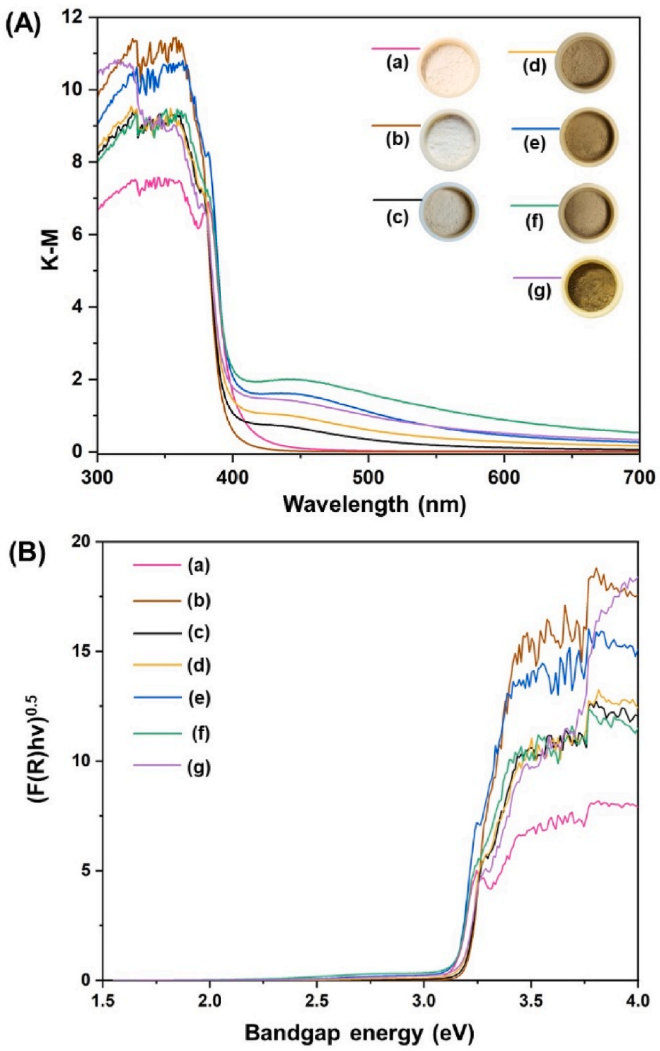

Fig. 9. (A) UV–Vis diffuse reflectance spectra and (B) Tauc plots of ZnO powder synthesized (a) without and with a 5-mL plant extract of *J. pseudosabina* and different concentrations of Ag: (b) 0 at%, (c) 0.1 at%, (d) 0.25 at%, (e) 0.5 at%, (f) 1 at%, and (g) 3 at%.

ZnO-Ag3 shows distinct Ag 3d peaks at 367.61 eV (Ag $3d_{3/2}$) and 373.52 eV (Ag $3d_{5/2}$), confirming the presence of Ag in its metallic form.

The experimental results obtained in this study are in good agreement with the DFT data reported previously by Thomas et al. (2012) They found that the Ag substitution at the Zn site (Ag_{Zn}) is the most stable, with a formation energy of 2.9 eV, and Ag can substitute Zn in both Zn-rich and O-rich environments. At the same time, the Ag substitution at the O site (Ag_O) is also possible only under Zn-rich conditions. However, interstitial Ag (Ag_i) has high formation energies (6.0 eV and 4.3 eV), suggesting it is unlikely to form. Li et al. (2011) also found that Ag preferentially substitutes Zn under both Zn-rich and O-rich conditions, with a low formation energy (0.91 eV) under O-rich conditions. At higher Ag concentrations (around 4 %), Ag tends to form a cluster on the surface rather than the core of ZnO, which aligns well with our findings.

The influence of Ag modification on the optical properties of ZnO was studied using UV–Vis diffuse reflectance spectroscopy. As shown in the UV–Vis diffuse reflectance spectra (Fig. 9A), non-modified ZnO-Ag0 has an absorption edge at approximately 389 nm, indicating electron excitation from the valence band to the conduction band of ZnO. With increasing the concentration of Ag, the absorption edge shifts to 450 nm, revealing enhanced visible light absorption. The optical bandgap energies determined from the Tauc plot (Fig. 9B) are reported in Table 2. It can be seen that, with increasing Ag concentration, the band gap values progressively decrease, from 3.16 eV with no Ag to a minimum of 3.10 eV with 1 % Ag content. This is consistent with the previous report (Sali and Sidarai, 2023). At 3 at% Ag, the optical bandgap energy slightly increases to 3.13 eV likely due to the phase segregation of metallic Ag. The powder color of the samples darkens with increasing the concentration of Ag, implying the modification of ZnO with Ag. Table 3 shows the surface charge of the various samples, revealing that all powders, irrespective of synthesis conditions and Ag doping, exhibit a negative charge, consistent with previous studies (Anupama et al., 2018; Waqif et al., 2024).

Table 2
Optical band gap values for different Ag-doped ZnO samples.

Sample	Band gap value (eV)
ZnO-Ag0	3.16
ZnO-Ag0.1	3.16
ZnO-Ag0.25	3.14
ZnO-Ag0.5	3.11
ZnO-Ag1	3.10
ZnO-Ag3	3.13

Table 3
Surface charge for ZnO samples prepared with different plant extract volumes and modified with Ag.

Sample name	Surface charge (mV)
ZnO-PE0	−28.86 ± 0.61
ZnO-PE1	−13.97 ± 0.16
ZnO-PE5	−17.60 ± 1.65
ZnO-PE10	−12.57 ± 0.72
ZnO-PE15	−15.07 ± 1.14
ZnO-PE20	−13.50 ± 1.30
ZnO-Ag0.1	−18.70 ± 2.65
ZnO-Ag0.25	−20.73 ± 2.66
ZnO-Ag0.5	−11.27 ± 2.64
ZnO-Ag1	−18.57 ± 2.55
ZnO-Ag3	−17.40 ± 2.11

3.2. *Antibacterial activity of ZnO synthesized using different plant extract volumes and Ag concentrations*

3.2.1. *Agar-based disk diffusion assay*

The antibacterial activities of non-modified and Ag-modified ZnO powder were tested against the Gram-positive *B. subtilis* 168 and the Gram-negative bacteria *E. coli* W3110 using an agar-based disk diffusion assay. The results are shown in Fig. 10, where the inhibition of bacterial growth around the ZnO-impregnated disks is indicated by darkened zones arising from the translucence of the black underlay. The measured diameters of these inhibition zones are listed in Fig. S6. The data shows the presence of inhibition zones for different samples of *B. subtilis* (Gram-positive) in comparison to *E. coli* (Gram-negative), as a more enhanced effect is observed for *B. subtilis*. The discrepancy in the antibacterial activities of the ZnO powder likely arises from the distinct structures of bacterial cell envelopes (Espitia et al., 2012). *B. subtilis* has a thick peptidoglycan layer with attached lipoteichoic and teichoic acids, whereas *E. coli* has an outer membrane with lipopolysaccharides (LPS), which acts as a permeability barrier for large molecules and water-insoluble compounds.

Zeta potential measurements revealed a negative surface charge of the samples, promoting interaction with the less negatively charged cell envelope of *B. subtilis*, resulting in cellular damage and bacterial death. The envelope of Gram-positive *B. subtilis* may enhance the penetration of reactive oxygen species (ROS), including hydroxyl radicals (•OH),

	Samples	Gram-positive bacteria *B. subtilis*	Gram-negative bacteria *E. coli*
1	ZnO NPs synthesized with plant extract volume variation	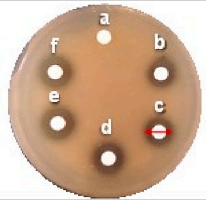	
2	ZnO NPs synthesized with different silver concentrations	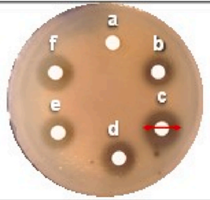	
3	ZnO NPs synthesized without plant extract	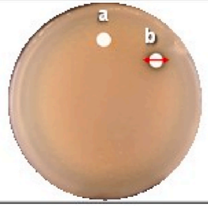	

Fig. 10. Agar-disk diffusion antibacterial assay of *B. subtilis* and *E. coli.* **1.** (a) DMSO, (b) ZnO-PE1, (c) ZnO-PE5, (d) ZnO-PE10, (e) ZnO-PE15, and (f) ZnO-PE20. **2.** (a) DMSO, (b) ZnO-Ag0.1, (c) ZnO-Ag0.25, (d) ZnO-Ag0.5, (e) ZnO-Ag1, and (f) ZnO-Ag3. **3.** (a) DMSO and (b) ZnO powder (ZnO-PE0) synthesized without plant extract.

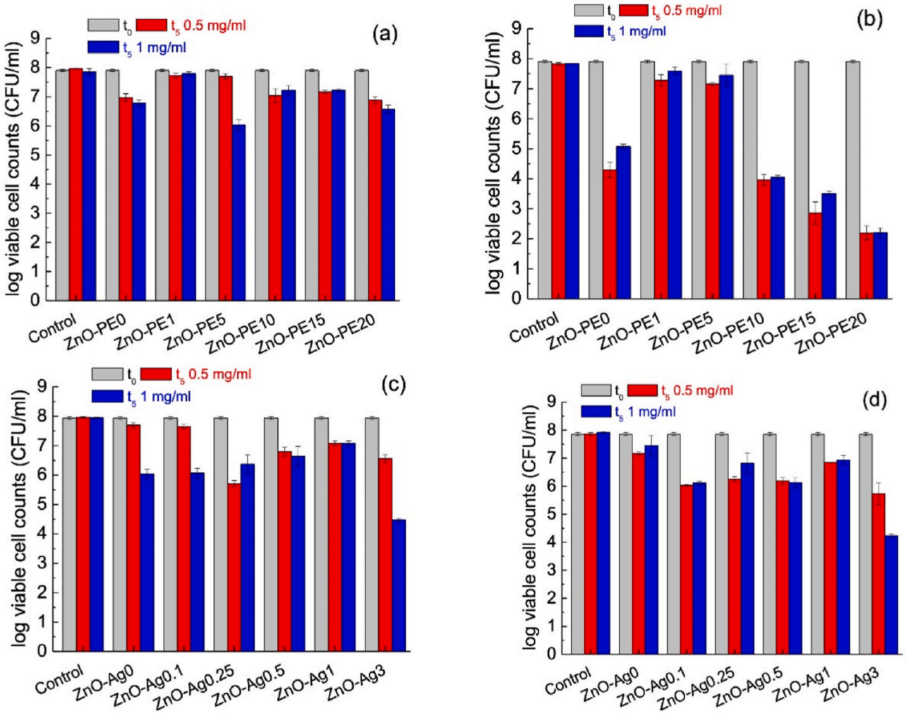

Fig. 11. Cell viability for *S. aureus* (a and c) and *E. coli* (b and d) in contact with undoped ZnO samples prepared with different plant extract volumes (a and b) and Ag-doped ZnO (c and d).

superoxide anions ($O_2^{-}\bullet$), and hydrogen peroxide (H_2O_2) (Hojamberdiev et al., 2013; Li et al., 2018; Nie et al., 2020), further contributing to bacterial inactivation. Previous studies have similarly reported higher ZnO efficacy against Gram-positive strains in disk diffusion assays (Espitia et al., 2012).

The ZnO powder synthesized using the plant extract of *J. pseudosabina* showed better antibacterial activity than its counterpart synthesized without using the plant extract. Particularly, ZnO-PE20 exhibited the largest inhibition zone (1.45 cm). Table 3 shows that the samples prepared with varying amounts of plant extracts exhibit no

Table 4
Concentrations of the Zn and Ag ions released during the antibacterial tests.

Sample name	Zn released (mg/L)	Ag released (mg/L)
ZnO-PE0	11.07 ± 0.85	–
ZnO-PE1	2.52 ± 1.19	–
ZnO-PE5	4.24 ± 0.95	–
ZnO-PE10	14.59 ± 0.82	–
ZnO-PE15	15.78 ± 2.58	–
ZnO-PE20	16.58 ± 1.18	–
ZnO-Ag0.1	6.98 ± 1.54	0.131 ± 0.042
ZnO-Ag0.25	1.59 ± 0.57	0.043 ± 0.016
ZnO-Ag0.5	3.47 ± 1.66	0.127 ± 0.036
ZnO-Ag1	1.86 ± 0.34	0.103 ± 0.025
ZnO-Ag3	5.57 ± 1.26	0.256 ± 0.011

significant differences in charge. Therefore, the enhanced antibacterial performance of ZnO-PE20 cannot be attributed to this factor. The higher antibacterial activity is likely due to its smaller particle size which can enhance bacterial penetration in the agar medium. Ag-modified ZnO samples exhibited improved antibacterial activity, and the ZnO-Ag0.25 (0.25 at% Ag) showed the highest inhibition zone of 1.65 cm among all samples, while the ZnO-Ag1 (1 at% Ag) and ZnO-Ag3 (3 at% Ag) had slightly reduced antibacterial activity possibly due to their larger particle sizes that limit internalization into bacterial cells.

3.2.2. *Viable plate count method*

Fig. 11 shows the results of viable plate count method experiments. Two different powder concentrations were employed, namely 0.5 and 1 mg/mL. Considering the undoped ZnO, it can be seen that the antimicrobial activity is affected by the preparation conditions. For *S. aureus* (Fig. 11a) the most effective sample is ZnO-PE5 (i.e. using 5 mL of extract). In fact, a decrease of just over two logarithmic units was registered (concentration of 1 mg/mL); this corresponds to a bacterial inactivation higher than 99 %. For the other samples, a smaller but noticeable antibacterial effect is observed, and for sample ZnO-PE20, a reduction of bacterial CFU of almost two units was seen. Moreover, this sample is more effective than ZnO-PE5 at lower concentrations; in fact, the difference between the activity at 0.5 and 1 mg/mL is non-significant. Considering the *E. coli* (Fig. 11b), on the other hand, a completely different behavior was observed. ZnO prepared without any extract, in fact, already exhibited significant antibacterial activity, resulting in approximately 99.99 % inactivation of bacteria, with a decrease of around 4 orders of magnitude. When a small amount of PE was employed (1 and 5 mL) the antibacterial activity was much smaller; in fact, the bacterial counts decreased by less than one logarithmic unit (about 65–80 %). For larger PE volumes, however, a much-enhanced antibacterial activity was observed; in particular with 20 mL of PE, the bacterial counts decreased by 6 orders of magnitude, corresponding to inactivation of 99.9999 % - a remarkable effect, which was observed also for 0.5 mg/mL concentration.

Table 4 shows the amount of Zn metal released during the 5 h incubation period; it can be seen that higher Zn release was observed for samples prepared with extract volume of 10 mL and higher, causing a more effective inactivation of *E. coli*. This is reasonable, since this strain has a negative charge (Alves et al., 2010), and, hence, it is more likely to interact with the released positive ions. With *S. aureus* there is not a direct correspondence between the released Zn ion and the bacteria inactivation; it has to be considered, however, that this strain has a less negative membrane (Espitia et al., 2012; Halder et al., 2015), which makes the interaction with the positive released ions less likely to take place. Moreover, the different composition of the bacterial membrane of the Gram-positive strain can also have an effect.

It is important to highlight that the mechanism involved in these liquid assays differs from that in the diffusion assays described above, as in liquid tests ion release is the primary factor influencing antibacterial activity. Conversely, in other types of assays, additional mechanisms may also play a significant role in determining the outcome (Biswas et al., 2022).

Considering Ag-doped ZnO (Fig. 11c and d), it can be seen that for *S. aureus* the addition of Ag does not always lead to a significant increase in the antibacterial activity; in some cases, on the contrary, a decrease was observed (i.e. for Ag concentration of 0.5 and 1 %). With the highest Ag concentration; however, a much more enhanced bacteria inactivation was observed, namely about 99.99 %. For *E. coli* a positive effect on bacteria inactivation can be seen even with the lowest Ag concentrations; even for this strain, however, the most pronounced effect was observed for the highest Ag concentration.

Data reported in Table 4 show that a relatively small amount of Ag is released. This is in agreement with XPS data which indicate that Ag is present in its metallic state. It is known that metallic Ag has very low solubility, lower than Ag in ionic form and this can significantly affect the antibacterial activity (Piccirillo et al., 2015; Lalueza et al., 2011).

The interactions between ZnO and Ag can modulate antibacterial activity through multiple mechanisms. In most cases, a synergistic effect is observed, resulting in enhanced antimicrobial efficacy. This enhancement arises from the intrinsic bactericidal properties of Ag, coupled with the increased generation of reactive oxygen species (ROS). However, under certain conditions, antagonistic effects may emerge, potentially mitigating the expected antibacterial enhancement. For

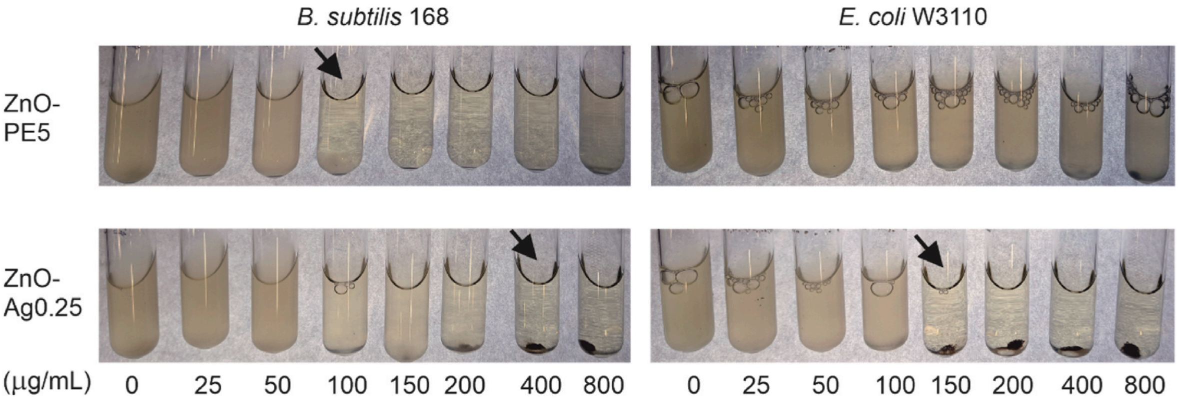

Fig. 12. Estimation of MICs. Liquid cultures of *Bacillus subtilis* 168 and *Escherichia coli* W3110 were grown overnight in LB and diluted 1000-fold in LB to give non-turbid suspensions with 2×10^6 and 6×10^6 CFU/mL, respectively. ZnO-PE5 and ZnO-Ag0.25, suspended in DMSO, were added (3.8–120 μL) to 3 mL of the bacterial suspensions in glass vials to give concentrations in the range of 25–800 μg/mL. Samples supplemented with 120 μL of DMSO served as controls. The vials were incubated overnight in a carousel shaker at 30 °C. Arrows indicate non-turbid vials with the lowest concentration of ZnO in a row which were considered as the estimates of the MICs.

instance, as reported by Kumar et al. (Vinod Kumar et al., 2017) the addition of Ag had a detrimental effect as it caused changes in the morphology and structure of ZnO nanoparticles, reducing their antibacterial effect. In another work by Lekoui et al. (2025), the antibacterial activity of ZnO films was not significantly affected by Ag doping. Considering the data of Tables 4 and it is interesting to see that Ag presence causes a decrease in the amount of Zn released; apart from sample ZnO-Ag3, this lower Zn solution concentration was not balanced by a sufficiently high Ag concentration – therefore overall, the antimicrobial efficiency was lower. For sample ZnO-Ag3, however, the higher Ag release led to an improved antibacterial performance. The more contained Zn release in the Ag-doped ZnO systems was previously reported in the literature. Indeed, significantly lower values were observed by Milisav et al. (2025), and the authors observed the same effect also for Cu-doped ZnO. It is proposed that metallic silver on the particle surface partially obstructs Zn dissolution. A previous study suggests that Ag addition to ZnO generally enhances antibacterial activity; thus, this approach was explored. In this study, undoped ZnO exhibited strong antibacterial performance against Gram-negative *E. coli* but lower efficacy against Gram-positive *S. aureus*. The doping aimed to improve the latter. This effect was evident at the highest Ag concentration; however, no similar trend was observed for *E. coli*. These results indicate that the incorporation of costly precious metals is warranted for applications targeting Gram-positive strains, whereas for Gram-negative strains, their addition provides no significant advantage.

3.2.3. Estimation of minimum inhibitory concentration (MIC)

To gain a closer insight into the concentration dependence of the antibacterial activity of the synthesized samples, the MICs against Gram-positive *B. subtilis* 168 and Gram-negative *E. coli* W3110 were estimated in liquid cultures using ZnO-PE5 (non-modified) and ZnO-Ag0.25 (Ag-modified), respectively. The results are shown in Fig. 12. The MICs against *B. subtilis*, defined as the lowest concentration of the synthesized samples that prevented a turbidity increase, were found to be 100 μg/mL for ZnO-PE5 and 400 μg/mL for ZnO-Ag0.25. To distinguish between bacteriostatic and bactericidal modes of action, aliquots of non-turbid samples after incubation at ZnO concentrations above the MIC were spread on LB agar plates. CFU/mL in all samples ranged below 0.01 % to 0.5 % relative to the CFU/mL prior to the addition of ZnO suspension. This finding suggested an interplay of bactericidal and bacteriostatic activity against *B. subtilis*, as a major portion of the cells was killed and survivors were unable to proliferate in the presence of ZnO in the liquid cultures. Bactericidal activity was observed in a similar way in the cell viability tests against Gram-positive *S. aureus* (Fig. 11), where ZnO-PE5 (at a concentration of 1 mg/mL) and ZnO-Ag.25 (0.5 mg/mL) reduced viable cell numbers by almost two and more than two orders of magnitude, respectively.

A comparison of ZnO-PE5-mediated inhibition of *E. coli* (MIC against strain W3110, Fig. 12; reduction of viable cell number of strains ATCC 25922, Fig. 11) seemingly gave inconsistent results at first glance. In repeated MIC assays, the final turbidity of the cultures was not markedly diminished by ZnO-PE5 at concentrations up to 0.8 mg/mL. In contrast, 0.5 mg/mL ZnO-PE5 reduced the viable cell number although not dramatically, but significantly. It is reasonable to assume that a portion of the cells was also killed in the liquid cultures during MIC testing. Moderate bacteriostatic efficiency, however, did not prevent the multiplication of the surviving cells, leading to turbid cultures upon overnight incubation. ZnO-Ag0.25 was found active against *E. coli* when permanently present in the liquid cultures for MIC determination (Fig. 12) and during the 5-h treatment prior to viable cell counting (Fig. 11). The MIC was estimated to be approximately 150 μg/mL. Approximately 5 % of cells incubated at the MIC or higher concentrations of ZnO-Ag0.25 remained viable, as indicated by colony formation upon incubation of aliquots on agar plates without the inhibitor. This result is concordant with the assumption of a combination of bacteriostatic and bactericidal inhibition of *E. coli* W3110. In comparison with *B. subtilis* 168, the bactericidal effect on *E. coli* W3110 was less pronounced.

4. Conclusions

Green synthesis of ZnO using *Juniperus pseudosabina* plant extract provides a sustainable alternative to conventional methods, eliminating the need for hazardous chemicals and pH adjustment. The proposed mechanisms of ZnO formation involve bioreduction and chelation, with chelation dominating at higher extract volumes, resulting in artichoke-like structures. Ag modification at 0.1–1 at% likely involves Ag $^{+}$ substitution for Zn^{2+}, while 3 at% Ag induces the formation of Ag^0 clusters on the ZnO surface. Among the synthesized samples, ZnO-PE20 and ZnO-Ag0.25 exhibited higher antibacterial activity against Gram-positive *B. subtilis*. Viable plate count assays confirmed the antibacterial efficacy, reducing the bacterial count of *S. aureus* from 9×10^7 CFU/mL to 6.38×10^6 CFU/mL and *E. coli* from 8.2×10^7 CFU/mL to 1.0×10^6 CFU/mL, achieving bacterial inactivation rates of 99.999 %. The utilization of plant-based resources such as *J.pseudosabina* aligns with principles of green chemistry, enhancing the biocompatibility and potential applicability of the resulting ZnO nanostructures in environmentally relevant domains such as antimicrobial coatings, water purification, and biomedical applications. This work underscores the feasibility of eco-conscious nanomaterial synthesis, advancing sustainable methodologies for functional material development.

CRediT authorship contribution statement

Zulfira Kurbanova: Writing – original draft, Visualization, Validation, Software, Methodology, Investigation, Funding acquisition, Formal analysis, Data curation, Conceptualization. **Sofia I.A. Pereira:** Writing – review & editing, Writing – original draft, Visualization, Validation, Methodology, Investigation, Funding acquisition, Formal analysis. **Ana S.S. Sousa:** Writing – original draft, Validation, Software, Methodology, Investigation, Formal analysis. **Clara Piccirillo:** Writing – original draft, Validation, Resources, Methodology, Investigation. **Ulugbek Shaislamov:** Writing – original draft, Visualization, Software, Methodology, Investigation. **Kunio Yubuta:** Writing – original draft, Visualization, Methodology, Investigation. **Katsuya Teshima:** Writing – original draft, Visualization, Software, Methodology, Investigation. **Thomas Eitinger:** Writing – review & editing, Writing – original draft, Visualization, Validation, Supervision, Methodology, Investigation, Formal analysis, Conceptualization. **Mirabbos Hojamberdiev:** Writing – review & editing, Writing – original draft, Visualization, Validation, Supervision, Resources, Methodology, Investigation, Data curation, Conceptualization.

Declaration of competing interest

The authors have declared no competing interest.

Acknowledgements

ZK would like to acknowledge the Erasmus Mundus Joint Master's Degree in Chemical Nanoengineering (CNE program) funded by the European Commission. The authors would like to thank Mr. Jens Michael Lassen from Humboldt-Universität zu Berlin, Germany, Ms. Reiko Shiozawa from Shinshu University, Japan, and Dipl. Phys. Christoph Fahrenson from ZELMI, TU Berlin, Germany, for their kind assistance with the MIC assays, XPS and SEM analyses, respectively. This work was partly supported by National Funds from FCT - Fundação para a Ciência e a Tecnologia through project UID/Multi/50016/2019. C.P. acknowledges the Italian Ministry of Research (MUR) under the complementary actions to the NRRP (PNC0000007) "Fit4MedRob- Fit for Medical Robotics" grant (contract number CUP B53C22006960001).

Appendix A. Supplementary data

Supplementary data to this article can be found online at https://doi.org/10.1016/j.jclepro.2025.145785.

Data availability

Data will be made available on request.

References

Aga, K.W., Efa, M.T., Beyene, T.T., 2022. Effects of sulfur doping and temperature on the energy bandgap of ZnO nanoparticles and their antibacterial activities. ACS Omega 7, 10796–10803.

Al-darwesh, M.Y., Ibrahim, S.S., Mohammed, M.A., 2024. A review on plant extract mediated green synthesis of zinc oxide nanoparticles and their biomedical applications. Results Chem. 7, 101368.

Al-Gaashani, R., Radiman, S., Daud, A.R., Tabet, N., Al-Douri, Y., 2013. XPS and optical studies of different morphologies of ZnO nanostructures prepared by microwave methods. Ceram. Int. 39, 2283–2292.

Alves, C.S., Melo, M.N., Franquelim, H.G., Ferre, R., Planas, M., Feliu, L., Bardají, E., Kowalczyk, W., Andreu, D., Santos, N.C., Fernandes, M.X., Castanho, M.A.R.B., 2010. *Escherichia coli* cell surface perturbation and disruption induced by antimicrobial peptides BP100 and pepR. J. Biol. Chem. 285, 27536–27544.

Anupama, C., Kaphle, A., Udayabhanu, Nagaraju, G., 2018. *Aegle marmelos* assisted facile combustion synthesis of multifunctional ZnO nanoparticles: study of their photoluminescence, photo catalytic and antimicrobial activities. J. Mater. Sci. Mater. Electron. 29, 4238–4249.

Babayevska, N., Przysiecka, Ł., Iatsunskyi, I., Nowaczyk, G., Jarek, M., Janiszewska, E., Jurga, S., 2022. ZnO size and shape effect on antibacterial activity and cytotoxicity profile. Sci. Rep. 12, 8148.

Basnet, P., Chanu, T.I., Samanta, D., Chatterjee, S., 2018. A review on bio-synthesized zinc oxide nanoparticles using plant extracts as reductants and stabilizing agents. J. Photochem. Photobiol., B 183, 201–221.

Biswas, A., Kar, U., Jana, N.R., 2022. Cytotoxicity of ZnO nanoparticles under dark conditions *via* oxygen vacancy dependent reactive oxygen species generation. Phys. Chem. Chem. Phys. 24, 13965–13975.

Devamani, R.H.P., Alagar, M., 2013. Synthesis and characterization of copper (II) hydroxide nanoparticles. Nano Biomed. Eng. 5, 116–120.

Espitia, P., Soares, N., Coimbra, J., Andrade, N., Cruz, R., Medeiros, E., 2012. Zinc oxide nanoparticles: synthesis, antimicrobial activity, and food packaging applications. Food Bioprocess Technol. 5, 1447–1464.

Gavrilenko, E.A., Goncharova, D.A., Lapin, I.N., Nemoykina, A.L., Svetlichnyi, V.A., Aljulaih, A.A., Mintcheva, N., Kulinich, S.A., 2019. Comparative study of physicochemical and antibacterial properties of ZnO nanoparticles prepared by laser ablation of Zn target in water and air. Materials 12, 186.

Greeshma, K.P., Thamizselvi, R., 2023. Phytogenic synthesis of ZnO nanoparticles from *Catharanthus Roseus* and *Morinda Citrifolia* leaf extract and its promising multifunctional biological applications. J. Drug Deliv. Sci. Technol. 87, 104785.

Halder, S., Yadav, K.K., Sarkar, R., Mukherjee, S., Saha, P., Haldar, S., Karmakar, S., Sen, T., 2015. Alteration of Zeta potential and membrane permeability in bacteria: a study with cationic agents. SpringerPlus 4, 672.

Hampe, H., Petit, R.J., 2010. Cryptic forest refugia on the “Roof of the World”. New Phytol. 185, 5–7.

Hojamberdiev, M., Katsumata, K.-i., Morita, K., Aldabe Bilmes, S., Matsushita, N., Okada, K., 2013. One-step hydrothermal synthesis and photocatalytic performance of $ZnWO_4/Bi_2WO_6$ composite photocatalysts for efficient degradation of acetaldehyde under UV light irradiation. Appl. Catal. A 457, 12–20.

Jaffri, S.B., Ahmad, K.S., 2019. Foliar-mediated ag:zno nanophotocatalysts: green synthesis, characterization, pollutants degradation, and *in vitro* biocidal activity. Green Process. Synth. 8, 172–182.

Janeiro, P., Brett, A.M.O., 2004. Catechin electrochemical oxidation mechanisms. Anal. Chim. Acta 518, 109–115.

Khorsand Zak, A., Abd Majid, W.H., Abrishami, M.E., Yousefi, R., 2011. X-ray analysis of ZnO nanoparticles by williamson-hall and size-strain plot methods. Solid State Sci. 13, 251–256.

Lalueza, P., Monzón, M., Arruebo, M., Santamaría, J., 2011. Bactericidal effects of different silver-containing materials. Mater. Res. Bull. 46, 2070–2076.

Lekoui, F., Amrani, R., Benalia, A., Belbahi, A., Zitouni, I., Garoudja, E., Filali, W., Manseri, A., Oussalah, S., Hassani, S., Ţălu, Ş., Henini, M., 2025. Ag-Doped ZnO nanostructured thin films for transparent antibacterial surfaces: effect of Ag content. Inorg. Chem. Commun. 173, 113831.

Li, W.-J., Shi, E.-W., Zhong, W.-Z., Yin, Z.-W., 1999. Growth mechanism and growth habit of oxide crystals. J. Cryst. Growth 203, 186–196.

Li, Y., Zhao, X., Fan, W., 2011. Structural, electronic, and optical properties of Ag-doped ZnO nanowires: first principles study. J. Phys. Chem. C 115, 3552–3557.

Li, N., Zhu, G., Hojamberdiev, M., Zhu, R., Chang, J., Gao, J., Guo, Q., Liu, P., 2018. Pd nanoparticle-decorated $Bi_4O_5Br_2$ nanosheets with enhanced visible-light photocatalytic activity for degradation of Bisphenol A. J. Photochem. Photobiol. A 356, 440–450.

Mahboub, S., Zerrouki, D., Henni, A., 2020. Green synthesis and characterization of silver nanoparticles using *Juniperus Communis* leaf extract: catalytic activity in real-outdoor conditions and electrochemical properties. Appl. Organomet. Chem. 34, e5956.

Makuła, P., Pacia, M., Macyk, W., 2018. How to correctly determine the band gap energy of modified semiconductor photocatalysts based on UV–Vis spectra. J. Phys. Chem. Lett. 9, 6814–6817.

Mardosaitė, R., Jurkevičiūė, A., Račkauskas, S., 2021. Superhydrophobic ZnO nanowires: wettability mechanisms and functional applications. Cryst. Growth Des. 21, 4765–4779.

Mërtiri, I., Păcularu-Burada, B., Stănciuc, N., 2024. Phytochemical characterization and antibacterial activity of Albanian *Juniperus Communis* and *Juniperus Oxycedrus* berries and needle leaves extracts. Antioxidants 13, 345.

Milisav, A.-M., Mičetić, M., Dubček, P., Sotelo, L., Cantallops-Vilà, C., Erceg, I., Fontanot, T., Bojanić, K., Fiket, Ž., Ivanić, M., Sarau, G., Christiansen, S., Meurice, E., Car, T., Sikirić, M.D., 2025. Effect of Ag and Cu doping on the properties of ZnO magnetron sputtered thin films for biomedical applications. Appl. Surf. Sci. 690, 162623.

Mintcheva, N., Aljulaih, A.A., Wunderlich, W., Kulinich, S.A., Iwamori, S., 2018. Laser-ablated ZnO nanoparticles and their photocatalytic activity toward organic pollutants. Materials 11, 1127.

Nie, J., Gao, J., Shen, Q., Zhang, W., Rao, F., Hojamberdiev, M., Zhu, G., 2020. Flower-like $Bi^0/CeO_{2-\delta}$ plasmonic photocatalysts with enhanced visible-light-induced photocatalytic activity for NO removal. Sci. China Mater. 63, 2272–2280.

Ong, W.-J., Tan, L.-L., Chai, S.-P., Yong, S.-T., Mohamed, A.R., 2014. Highly reactive {001} facets of TiO_2 -based composites: synthesis, formation mechanism and characterization. Nanoscale 6, 1946–2008.

Piccirillo, C., Pullar, R.C., Tobaldi, D.M., Lima Castro, P.M., Estevez Pintado, M.M., 2015. Silver-containing calcium phosphate materials of marine origin with antibacterial activity. Ceram. Int. 41, 10152–10159.

Rajendran, R., Mani, A., 2020. Photocatalytic, antibacterial and anticancer activity of silver-doped zinc oxide nanoparticles. J. Saudi Chem. Soc. 24, 1010–1024.

Sali, R.K., Sidarai, A.H., 2023. Antimicrobial activity and cytotoxic effect of ZnO and Ag-ZnO nanoparticles using *Capsicum frutescens* fruits. BioNanoScience 13, 153–166.

Sampath, S., Bhushan, M., Saxena, V., Pandey, L.M., Singh, L.R., 2022. Green synthesis of Ag doped ZnO nanoparticles: study of their structural, optical, thermal and antibacterial properties. Mater. Technol. 37, 2785–2794.

Scherrer, P., 1918. Bestimmung der Größe und der inneren Struktur von Kolloidteilchen mittels Röntgenstrahlen. EUDML 2, 98–100.

Serwecińska, L., 2020. Antimicrobials and antibiotic-resistant bacteria: a risk to the environment and to public health. Water 12, 3313.

Sirelkhatim, A., Mahmud, S., Seeni, A., Kaus, N.H.M., Ann, L.C., Bakhori, S.K.M., Hasan, H., Mohamad, D., 2015. Review on zinc oxide nanoparticles: antibacterial activity and toxicity mechanism. Nano-Micro Lett. 7, 219–242.

Stan, M., Popa, A., Toloman, D., Toloman, D., Silipas, T.-D., Vodnar, D.C., 2016. Antibacterial and antioxidant activities of ZnO nanoparticles synthesized using extracts of *Allium Sativum, rosmarinus officinalis* and *Ocimum Basilicum*. Acta Metall. Sin. 29, 228–236.

Talebian, N., Amininezhad, S.M., Doudi, M., 2013. Controllable synthesis of ZnO nanoparticles and their morphology-dependent antibacterial and optical properties. J. Photochem. Photobiol., B 120, 66–73.

Tesfaye, M., Gonfa, Y., Tadesse, G., Temesgen, T., Periyasamy, S., 2023. Green synthesis of silver nanoparticles using *Vernonia Amygdalina* plant extract and its antimicrobial activities. Heliyon 9, e17356.

Thomas, M.A., Sun, W.W., Cui, J.B., 2012. Mechanism of Ag doping in ZnO nanowires by electrodeposition: experimental and theoretical insights. J. Phys. Chem. C 116, 6383–6391.

Upadhyaya, H., Shome, S., Sarma, R., Tewari, S., Bhattacharya, M.K., Panda, S.K., 2018. Green synthesis, characterization and antibacterial activity of ZnO nanoparticles. Am. J. Plant Sci. 9, 1279–1291.

Vinod Kumar, J., Prakash, J., Singh, J.P., Chae, K.H., Swart, C., Ntwaeaborwa, O.M., Swart, H.C., Dutta, V., 2017. Role of silver doping on the defects related photoluminescence and antibacterial behavior of zinc oxide nanoparticles. Colloids Surf. B Biointerfaces 159, 191–199.

Volnianska, O., Boguslawski, P., Kaczkowski, J., Jakubas, P., Jezierski, A., Kaminska, E., 2009. Theory of doping properties of Ag acceptors in ZnO. Phys. Rev. B 80, 245212.

Wang, D., Jiang, H., Zong, X., Xu, Q., Ma, Y., Li, G., Li, C., 2011. Crystal facet dependence of water oxidation on $BiVO_4$ sheets under visible light irradiation. Chem. Eur J. 17, 1275–1282.

Waqif, H., Munir, N., Farrukh, M.A., Hasnain, M., Sohail, M., Abideen, Z., 2024. Algal macromolecular mediated synthesis of nanoparticles for their application against citrus canker for food security. Int. J. Biol. Macromol. 263, 130259.

Yubuta, K., Sato, T., Nomura, A., Haga, K., Shishido, T., 2007. Structural characterization of ZnO nano-chains studied by electron microscopy. J. Alloys Compd. 436, 396–399.

Zhao, Y., Li, R., Mu, L., Li, C., 2017. Significance of crystal morphology controlling in semiconductor-based photocatalysis: a case study on $BiVO_4$ photocatalyst. Cryst. Growth Des. 17, 2923–2928.

Zhi Zing, Z., Talip, N., Chin Fhong, B.A., Ainuddin, A.R., Basri, H., 2022. Polyphenol-mediated green synthesis of zinc oxide and their antibacterial properties: a novel size-controlled approach. Malays. J. Anal. Sci. 26, 884–901.